Chlorophyll production in the Amundsen Sea boosts heat flux to atmosphere and weakens heat flux to ice shelves

A G Twelves[1,2], D N Goldberg[2], P R. Holland[3], S F Henley[2], M R Mazloff[4], D C Jones[3,5]

[1]Finnish Meteorological Institute, Helsinki, Finland

[2]School of GeoSciences, University of Edinburgh, Edinburgh, United Kingdom

[3]British Antarctic Survey, NERC, UKRI, Cambridge, United Kingdom

[4]Scripps Institution of Oceanography, La Jolla, California

[5]Cooperative Institute for Great Lakes Research, University of Michigan, Ann Arbor, Michigan

Corresponding author: A G Twelves, `andrew.twelves@fmi.fi`

Abstract

The Amundsen Sea in West Antarctica features rapidly thinning ice shelves and large, seasonally recurring polynyas. Within these polynyas, sizable spring phytoplankton blooms occur. Although considerable effort has gone into characterising heat fluxes between the Amundsen Sea, its associated ice shelves, and the overlying atmosphere, the effect of the phytoplankton blooms on the distribution of heat remains poorly understood. In this modelling study, we implement a feedback from biogeochemistry onto physics into MITgcm-BLING and use it to show, for the first time, that high levels of chlorophyll – concentrated in the Amundsen Sea Polynya and the Pine Island Polynya – accelerate springtime surface warming in polynyas through enhanced absorption of solar radiation. The warm midsummer anomaly (on average between $+0.2°C$ and $+0.3°C$) at the surface is quickly dissipated to the atmosphere, by small increases in latent and longwave heat loss as well as a substantial (17.5%) increase in sensible heat loss from open water areas. The summertime warm anomaly also reduces the summertime sea ice volume, and stimulates enhanced seasonal melting near the fronts of ice shelves. However larger effects derive from the accompanying cold anomaly, caused by shading of deeper waters, which persists throughout the year and affects a decrease in the volume of Circumpolar Deep Water on the continental shelf. This cooling ultimately leads to an increase in wintertime sea ice volume, and reduces basal melting of Amundsen Sea ice shelves by approximately 7% relative to the model scenario with no phytoplankton bloom.

Plain Language Summary

Near the Antarctic coastline the sea ice cover is broken by patches of open water, called polynyas, which often undergo a visible change in colour from blue to green as spring progresses. This is due to the chlorophyll produced in blooms of microscopic algae. Here we use computer simulations to investigate the impact of this change in colour on the delicate system of ice and ocean in the Amundsen Sea region of west Antarctica. We find that the 'greening' of polynyas helps to trap more of the sun's energy close to the sea surface, but that this excess heat is then released back to the atmosphere over the course of the summer. Meanwhile, the deeper waters of the polynya are exposed to less energy from the sun and therefore are cooler than they would be if there were no algae bloom. Ultimately, the cooling of deep waters across the Amundsen Sea weakens the transport of heat towards the continent. Our computer simulations show that, as a result, ice shelves

melt at a slightly slower rate when large algae blooms are present compared to when the surface waters are clear.

Key Points

1. We implement a feedback from biogeochemistry onto physics in MITgcm-BLING for the first time.
2. Chlorophyll induced warming at the surface is short-lived, with excess heat rapidly lost to the atmosphere.
3. Sub-surface cooling is persistent and leads to reduced melting from ice shelves.

1 Introduction

The west Antarctic coastline is characterised by annually recurring areas of open water – polynyas – within the sea ice pack. In the Amundsen Sea there are two such coastal polynyas, both of which host large spring phytoplankton blooms [*Arrigo and Van Dijken*, 2003; *Arrigo et al.*, 2012; *Park et al.*, 2017]. The Amundsen Sea Polynya (ASP) forms downwind of a line of icebergs grounded on Bear Ridge, and is bounded to the south by the front of Dotson Ice Shelf (DIS). The Pine Island Polynya (PIP) forms within Pine Island Bay and abuts the fronts of the Cosgrove and Thwaites Glacier Ice Shelves (TGIS) as well as the Pine Island Glacier Ice Shelf (PIGIS). Each of these ice shelves shows signs of thinning and/or grounding line retreat in satellite observations [*Christie et al.*, 2016; *Gourmelen et al.*, 2017; *Shepherd et al.*, 2019; *Shean et al.*, 2019], whilst the two polynyas exhibit exceptionally high primary productivity [*Arrigo and Van Dijken*, 2003; *Arrigo et al.*, 2015; *Alderkamp et al.*, 2012]. In this modelling study we investigate the effect of the spring phytoplankton bloom on heat fluxes from polynyas to the atmosphere and from the ocean to ice shelf fronts.

The deepest waters in the Amundsen Sea consist of Antarctic Bottom Water (AABW), originating from the Ross Sea to the west, and Circumpolar Deep Water (CDW), originating in the Antarctic Circumpolar Current [*Bai et al.*, 2022]. Both these water masses arrive at the Amundsen Sea via a small number of troughs at the continental shelf break. Mixing of CDW on the shelf produces a modified Circumpolar Deep Water (mCDW) mass, which ultimately flows into ice shelf cavities and stimulates basal melting [*Jacobs et al.*, 1992; *Arneborg et al.*, 2012]. Rising buoyant meltwater in turn generates an overturn-

ing circulation - the meltwater pump - within ice shelf cavities which pulls dissolved iron from depth to the surface [*Oliver et al.*, 2019; *Twelves et al.*, 2020; *Dinniman et al.*, 2020]. Above the warm and saline mCDW layer there is a cold and slightly less saline Winter Water (WW) layer, and above that a seasonally warmed layer of fresh Antarctic Surface Water (AASW).

Ocean stratification within the ASP and PIP is sensitive to summertime insolation and to inputs of ice shelf meltwater, which both tend to stabilise the water column, and to winds, which tend to destabilise the water column. The latter effect occurs both directly through wind stress and indirectly by driving a net export of freshwater in wind-blown sea ice [*Bett et al.*, 2020; *Zheng et al.*, 2021]. This stratification in turn impacts phytoplankton growth, with springtime stability helping to alleviate light limitation, before mixing in autumn and winter resupplies nutrients – most crucially iron – from depth before the next growth season [*St-Laurent et al.*, 2017]. Whilst vertical mixing is a dominant source of iron to other Antarctic seas, in the Amundsen Sea it plays a secondary role relative to the iron associated with ice shelf melting. [*Oliver et al.*, 2019; *Twelves et al.*, 2020; *Dinniman et al.*, 2020].

Numerous studies have investigated the role of Amundsen Sea ice shelves in stimulating phytoplankton growth – using in-situ measurements [*Gerringa et al.*, 2012; *Yager et al.*, 2016], satellite data [*Arrigo and Van Dijken*, 2003; *Park et al.*, 2017], and biogeochemical modelling [*St-Laurent et al.*, 2019; *Oliver et al.*, 2019; *Twelves et al.*, 2020]. Less attention has been paid to the effect that very high summer chlorophyll concentrations – locally up to 10 mg L^{-1} – have on the attenuation of shortwave radiation, and thus on the heat available to drive basal melting.

The important contribution of chlorophyll to ocean heat fluxes was initially demonstrated in coarse global models of the ocean [*Manizza et al.*, 2005]. Subsequent studies have included this 'bio-optical feedback' in regional models and with a focus on different aspects of the heat budget. Implementation in tropical regions [*Hernandez et al.*, 2017] showed a cooling of waters upwelling from depth, whilst other studies, extended to include the effects of coloured dissolved organic matter (CDOM), have shown reduced Arctic sea ice cover [*Pefanis et al.*, 2020] and increased heat fluxes to the atmosphere from the Baltic Sea [*Cahill et al.*, 2023]. This feedback remains important in coupled ocean-atmosphere

104 models, with phytoplankton blooms shown to impact storm tracks [*Gnanadesikan et al.*,

105 2010] and marine heatwaves [*Gnanadesikan et al.*, 2019].

106 However, until now, this feedback from biology onto physics has been disregarded in mod-

107 els of the Amundsen Sea and, to our knowledge, in ice shelf modelling more generally.

108 Instead, even state-of-the-art models represent shortwave attenuation using spatially ho-

109 mogeneous and time-invariant extinction coefficients. Commonly the surface waters are

110 assumed to absorb light to a similar degree as surface waters in oligotrophic regions, even

111 where observations and/or biogeochemical models show intense chlorophyll production

112 close to ice shelves during the spring and summer. As a result, shortwave radiation to-

113 wards the base of the mixed layer is systematically overestimated, and these ice-ocean

114 models include an artificial source of heat in this part of the water column.

115 One solution to this problem is to include the attenuation coefficient as an additional

116 free parameter when tuning ice-ocean models to accurately reproduce basal melt rates.

117 However it is already well established that the attenuation of light correlates strongly

118 with chlorophyll in the Southern Ocean [*Dutkiewicz et al.*, 2015], and moreover that at-

119 tenuation shows strong seasonal variation as a result.

120 Another approach is to use surface chlorophyll data – derived from satellite measurements

121 of ocean colour – as an additional input to the model. However, since satellite imagery

122 only captures the ocean surface, this requires an additional step in extrapolating surface

123 attenuation over the entire euphotic zone. Furthermore, using chlorophyll data to drive

124 the model introduces a potential mismatch between the chlorophyll concentration used

125 as forcing for the model and those aspects of the model dynamics (sea ice retreat, changes

126 to stratification) which would in fact be required for phytoplankton growth.

127 In this study we seek instead to quantify the net contribution of chlorophyll to the ice-

128 ocean system via a two-way coupling of MITgcm to the Biology Light Iron Nutrients and

129 Gases (BLING) model. Chlorophyll output from the biogeochemical model is used at

130 every time step to calculate the vertical distribution of shortwave heating in the phys-

131 ical model. Whilst entailing a higher computational cost, this approach captures the sea-

132 sonality of the euphotic depth and ensures that it is consistent with the seasonality of

133 the hydrodynamic model. Furthermore, this strategy allows us to make an entirely novel

134 quantitative estimate for the impact of a biological process - the iron-limited growth of

phytoplankton - on the heat fluxes between atmosphere, sea ice, and ice shelves in the Amundsen Sea.

2 Methods

2.1 Modelling Rationale

We integrate the *Manizza et al.* [2005] formulation for attenuation by chlorophyll into the thermodynamics of MITgcm, using the Biology Light Iron Nutrients and Gases (BLING) model to simulate biogeochemical processes [*Galbraith et al.*, 2010]. We apply this two-way coupled model to a domain covering the entire Amundsen Sea, and focus our attention on air-sea heat fluxes, sea ice and basal melting on the continental shelf. We choose to compare a model run with chlorophyll generated by BLING to a model run with zero chlorophyll, emphasizing two key points:

- Existing models of the Amundsen Sea (and other parts of the Antarctic continental shelf) contain an implicit contribution of chlorophyll (generally a substantial underestimate) in the form of water type [*Jerlov*, 1976]. Thus the changes we observe are not equivalent to the error in existing model setups, which have themselves been tuned using a water-type setup from the start. Instead they represent the sensitivity of the model, as tuned, to the addition or removal of chlorophyll.
- In the real world, entirely chlorophyll-free summertime conditions do not and will not occur in the Amundsen Sea. Thus our results do not represent forecasts but should instead be understood as quantifying the contribution of chlorophyll to ice-ocean heat fluxes, and as a demonstration of a hitherto neglected two-way coupling between ice shelves and phytoplankton blooms.

Our approach – quantifying the contribution of a water constituent to attenuation using a zero case as control – is similar to that taken by *Gnanadesikan et al.* [2019] in quantifying the impact of coloured dissolved organic matter (CDOM) on extreme sea surface temperatures.

2.2 Physical Model

We simulate ice-ocean interactions with the Massachusetts Institute of Technology general circulation model (MITgcm checkpoint 67c; *Marshall et al.* [1997]), including the

164   packages for sea ice [*Losch et al.*, 2010] and for static ice shelves [*Losch*, 2008]. Verti-

165   cal mixing – an important control on biogeochemical processes – is represented using the

166   K-profile parameterization (KPP) developed by *Large et al.* [1994].

167   Our domain contains several ice shelves, from Getz Ice Shelf in the west to Abbott Ice

168   Shelf in the east (Figure 1), and stretches north beyond the continental shelf break. Hor-

169   izontal resolution decreases from 2.8 km at the coastline to 5.2 km at the northern bound-

170   ary, whilst vertical resolution decreases from 10 m at the surface to 200 m in the deep-

171   est layer. Both our bathymetry and our ice shelf topography are based on BedMachine

172   Version 1 [*Morlighem et al.*, 2020]. However, as in *St-Laurent et al.* [2017] and *Bett et al.*

173   [2020], we also include a grounded iceberg "wall" northwards of Bear Island, which blocks

174   westward advection of sea ice. This feature has been shown to be important both for ac-

175   curate representation of the physical system [*Bett et al.*, 2020] and for simulating the spring

176   phytoplankton bloom in the ASP [*Twelves et al.*, 2020]. In addition, we prescribe a fresh-

177   water flux over the upper 300 m close to the coastline, intended to represent drifting ice-

178   bergs.

179   We source boundary conditions for temperature and salinity from the World Ocean At-

180   las climatology [*Locarnini et al.*, 2018; *Zweng et al.*, 2019], and for velocities from the

181   B-SOSE state estimate [*Verdy and Mazloff*, 2017]. B-SOSE also provides us with bound-

182   ary conditions for sea ice (concentration, thickness, velocity, and snow depth). We de-

183   rive our atmospheric forcing from the ERA5 reanalysis (1979-2018; [*Hersbach et al.*, 2020]).

184   This domain was first described in *Assmann et al.* [2013], where it was used to simulate

185   conditions in the Amundsen Sea since the first oceanographic observations were conducted

186   there in 1994. It was then further developed and validated in *Kimura et al.* [2017] and

187   *Bett et al.* [2020]. Using outputs from an ensemble of earth system models as forcing,

188   *Naughten et al.* [2022] were able to apply the same model setup to investigate changes

189   in the Amundsen Sea since the early twentieth century. *Naughten et al.* [2022] reported

190   a reduction in instances of convective cooling on the continental shelf over this period.

191   However the model also has a tendency to undergo periods of convection close to ice shelf

192   fronts in recent years, conflicting with observations.

193   For the remainder of this study we refer to these instances of convection in the model

194   as 'anachronistic convection periods', since they disagree with contemporary observa-

195   tions but may be representative of past Amundsen Sea conditions. These periods may

also be viewed as loosely representative of conditions at those locations around Antarctica where convection is currently observed. Thus, while we discard any anachronistic convection periods from our core analysis, we nonetheless share these results, as a means of widening the scope of our study beyond the Amundsen Sea continental shelf.

Our setup is closest to that used by *Goldberg et al.* [2023], who describe several key differences with the setup used by *Naughten et al.* [2022]. In the present study we introduce phytoplankton blooms to the model, via a modified coupling of MITgcm to the Biology Light Iron Nutrients and Gases (BLING) model [*Galbraith et al.*, 2010].

2.3 Biogeochemical Model

Previous work has shown that BLING is able to reproduce iron-light colimited phytoplankton blooms, both in the Amundsen Sea [*Twelves et al.*, 2020] and elsewhere [*Galbraith et al.*, 2010; *Castro de la Guardia et al.*, 2019]. In this study, as in *Twelves et al.* [2020], we employ an additional tracer for advected biomass in addition to the eight core tracers (dissolved inorganic carbon (DIC), total alkalinity, oxygen, nitrate, phosphate, iron, dissolved organic nitrogen (DON) and dissolved organic phosphorus (DOP)). Again following *Twelves et al.* [2020], as well as *St-Laurent et al.* [2019], we prescribe a concentration of 20 μmol m^{-3} for iron dissolved in glacial meltwater. The remaining tracers are neither sourced from nor diluted by glacial meltwater in our setup. Similarly we do not include the effects of sea ice or atmospheric deposition on tracer concentrations.

Starting from a a seasonal climatology of BSOSE (2008-2012 solution, *Verdy and Mazloff* [2017]), we generate lateral boundary conditions for each of the eight core tracers. For the additional tracer representing advected biomass we instead relax the tracer to zero at the boundaries. Incoming photosynthetically available radiation (PAR) is calculated within the model as 40% of the total incoming shortwave radiation (from the ERA5 reanalysis).

After first spinning up the physical model from 1 January 1979 (with initial condition itself seeded from a preliminary 24 year run), we deploy passive tracers from 1 January 1995. From 1 January 2003 we enable BLING and at the same time switch the shortwave attenuation scheme from one based on Jerlov water type [*Jerlov*, 1976] to one which treats water molecules and chlorophyll separately. We spin up each of the following ex-

226 periments for a further five years, before analysing the outputs from 1 January 2008 to
227 31 December 2014.

228 For the *GREEN* experiment we include large and small classes of phytoplankton, which
229 are treated separately in BLING but whose aggregate forms the biomass tracer advected
230 around the domain [*Twelves et al.*, 2020; *Verdy and Mazloff*, 2017]. The large class rep-
231 resent diatoms, whilst the small class represents *Phaeocystis antarctica*; together these
232 have been observed to constitute the large majority of biomass in the Amundsen Sea [*Lee
233 et al.*, 2022]. We account for the higher iron requirement of *P. antarctica* compared to
234 diatoms by allocating the former a half saturation constant of 0.2μmol m^{-3} and the lat-
235 ter a half saturation constant of 0.15μmol m^{-3} (following *Nissen and Vogt* [2021]).

236 For the *BLUE* experiment we artificially set the growth rate to zero for both phytoplank-
237 ton classes, leaving only a very small detrital biomass to be advected around the domain.
238 This detritus is several orders of magnitude smaller than the biomass in *GREEN*, so
239 we can consider *BLUE* to represent chlorophyll-free conditions in the Amunsdsen Sea.
240 The difference in outputs $GREEN-BLUE$ thus provides us with a proxy with which
241 to quantify the impact of chlorophyll on shortwave heating and on the ice-ocean system
242 as a whole.

2.4 Shortwave heating

244 In the Jerlov water type formulation [*Jerlov*, 1976], used by default in MITgcm and also
245 in the spin up of our model prior to 2003, attenuation of light is homogeneous in both
246 time and space. Each water type corresponds to a single attenuation profile represent-
247 ing a different mixture of optically active constituents, without explicitly resolving any
248 one of those constituents.

249 The Jerlov water type approach is characterised by simplicity. Just three numbers are
250 required to uniquely specify each type: an attenuation constant for visible light, an at-
251 tenuation coefficient for near-infrared light, and the ratio of the two components in the
252 incoming power spectrum. Previous modelling of the Amundsen Sea [*Kimura et al.*, 2017;
253 *Naughten et al.*, 2022; *Goldberg et al.*, 2023] with MITgcm assumed Jerlov water type
254 IA, representing relatively clear waters.

255 However, as argued above, the use of Jerlov water type is in fact unsuitable for the Amund-

256 sen Sea. In this study we instead use the *Manizza et al.* [2005] formulae for shortwave

257 attenuation in the physical model. These are the same equations previously implemented

258 in BLING to calculate PAR for phytoplankton by *Twelves et al.* [2020]. Our approach

259 here diverges from the Jerlov water-type approach in two ways. Firstly, the visible part

260 of the spectrum I_{vis} is divided into two components (I_{red}, I_{bg}) with equal power at the

261 surface but with different attenuating properties in seawater:

$$I_{vis} = I_{red} + I_{bg}; \tag{1}$$

262 where

$$\frac{\partial I_{red}}{\partial z} = -\kappa_{red}(z)I_{red}(z) \tag{2}$$

263 and

$$\frac{\partial I_{bg}}{\partial z} = -\kappa_{bg}(z)I_{bg}(z). \tag{3}$$

264 Secondly, and more importantly for our study, the attenuation coefficients (κ_{red}, κ_{bg})

265 for the two light bands are expressed as sums of contributions from water molecules and

266 from the chlorophyll concentrations calculated in BLING:

$$k_{red} = k_{red}^0 + \chi_{red}[Chl]^{e_{red}}; \tag{4}$$

$$k_{bg} = k_{bg}^0 + \chi_{bg}[Chl]^{e_{bg}}. \tag{5}$$

267 Here k_{red}^0, k_{bg}^0, χ_{red}, χ_{bg}, e_{red} and e_{bg} are constants as in *Twelves et al.* [2020]. Atten-

268 uation by other optically active constituents of seawater, such as CDOM or detritus, is

269 not resolved in BLING and thus is excluded from this study.

270 By extending this light attenuation scheme from BLING (where it affects the PAR avail-

271 able to phytoplankton, [*Twelves et al.*, 2020]) to the physical model, we achieve consis-

272 tency between the physical and biogeochemical models, and allow the latter to feed back

onto the former. The attenuation of shortwave radiation contributes to the heat budget in MITgcm, and thus the distribution of phytoplankton growth affects the distribution of heat.

Chlorophyll can also directly affect the albedo at the sea surface [*Yu et al.*, 2022]. However in our modelling study we keep ocean albedo constant, so that the only direct impact of chlorophyll on physics is via the attenuation of radiation in the ocean interior. This in turn changes the distribution of heat, which alters the sea ice distribution and air-sea heat fluxes.

2.5 Surface heat fluxes

The air-sea heat balance in MITgcm comprises both radiative (i.e., shortwave, longwave) and turbulent (i.e., sensible, latent) heat fluxes.

The shortwave heat flux *per unit area* at the surface F_{SW} is sensitive only to the external forcing SW_{down} and to the sea ice coverage. In ice-free seas, the incoming shortwave is modified only by the water albedo α_{ocean}, which is fixed (at a value of 0.1) in our model setup:

$$F_{SW} = (1 - \alpha_{ocean})SW_{down}. \tag{6}$$

The distribution of this heating over the water column then depends on the attenuation profile, which in turn is determined by chlorophyll concentration as described above.

In contrast the longwave heat flux *per unit area* F_{LW} comprises not only the incoming forcing LW_{down} but also the outgoing flux. The latter is calculated via a Stefan-Boltzmann law depending on the sea surface temperature T_{SURF},

$$F_{LW} = LW_{down} - \sigma T_{SURF}^4, \tag{7}$$

where σ is the Stefan-Boltzmann constant.

The sensible heat flux *per unit area* in MITgcm is calculated as

$$F_{SEN} = \rho_{atm}c_{p_{atm}}u_s c_u c_T \Delta T \tag{8}$$

295 where ρ_{atm} is the atmospheric density, u_s is the wind speed and ΔT is the difference be-

296 tween sea surface and atmospheric temperatures. The calculation of the bulk exchange

297 coefficients c_u and c_T follows *Bryan et al.* [1996], and $c_{p_{atm}}$ is equal to the specific heat

298 capacity at atmospheric pressure.

299 Similarly the latent heat flux *per unit area* is given by

$$F_{LAT} = \rho_{atm} L u_s c_u c_q \Delta q \tag{9}$$

300 where L is the latent heat of vaporzation, Δq is the difference between atmospheric hu-

301 midity and the saturated humidity, and c_q is an additional bulk exchange coefficient [*Bryan*

302 *et al.*, 1996]. These coefficients and fluxes are solved iteratively at each time step within

303 MITgcm.

304 On the Amundsen Sea continental shelf, the total area-integrated heat flux at the ocean

305 surface can be separated into a component $\mathbb{F}_{SICE}$ representing ice-covered sea surface,

306 and a component $\mathbb{F}_{OPEN}$ representing ice-free – polynya – model sea surface.

$$\mathbb{F}_{SURF} = \mathbb{F}_{SICE} + \mathbb{F}_{OPEN} \tag{10}$$

307 The term $\mathbb{F}_{SICE}$ includes contributions from the formation and melting of sea ice, as well

308 as fluxes within leads between the ice floes. Accordingly, the MITgcm ocean heat cal-

309 culations account both for the effect of sea ice cover in obstructing air-sea fluxes and for

310 the additional fluxes into and out of the sea ice itself. A full analysis of the MITgcm sur-

311 face heat budget in partially ice covered seas would require a detailed breakdown of the

312 heat fluxes between air and sea ice. Since theses are not provided as model diagnostics

313 within the MITgcm, their calculation would demand changes to the model code that are

314 beyond the scope of this study. Previous work with MITgcm on the components of the

315 wider Southern Ocean heat budget discounted $\mathbb{F}_{SICE}$ by masking out a fixed region of

316 the domain [*Tamsitt et al.*, 2016], but this would be unsuitable at the scale of our study,

317 where there is substantial interannual variability in the extent of coastal polynyas. In-

318 stead we use monthly outputs of the sea ice concentration, set a threshold of 10% cov-

319 erage to distinguish $\mathbb{F}_{SICE}$ from $\mathbb{F}_{OPEN}$, and only calculate the components of the air-

320 sea flux for the latter.

For an entirely ice-free portion of sea surface, $\mathbb{F}_{OPEN}$ is simply the sum of longwave, shortwave, sensible and latent heat fluxes:

$$\mathbb{F}_{OPEN} = \mathbb{F}_{LAT} + \mathbb{F}_{SENS} + \mathbb{F}_{LW} + \mathbb{F}_{SW} \tag{11}$$

where the blackboard bold font $\mathbb{F}$ is used to emphasise that the units are now integrated to W rather than Wm^{-2}, with all terms dependent on the size of the open water area.

3 Results

3.1 Chlorophyll and light

Figure 1 shows that early summertime light attenuation (in $GREEN$) is substantially increased within both the ASP and the PIP (relative to other ice-free regions). The euphotic depth - defined here as the depth where the light level is 1% of that immediately below the sea surface - is greater than 60 m for most of the ice-free portion of the domain, both north of the ice cover and in Eltanin Bay to the east of Abbot Ice Shelf. In the totally chlorophyll-free waters in $BLUE$ it is equal to around 140 m.

In the ASP and the PIP the euphotic layer is generally shallower than 50 m and in places shallower than 40 m. This spatial pattern is due to the high concentrations of chlorophyll which are generated in the spring phytoplankton blooms close to Dotson Ice Shelf and Pine Island Glacier.

The model simulations show an anachronistic convection period starting in 2013 and continuing through 2014. We highlight this in Figure 1 b, which shows a thick layer of CDW (temperature $> 0°C$) in Pine Island Bay (the sub-domain demarcated with a dashed line in Figure 1) from 2008 to 2012, which then collapses entirely during 2013. We emphasize the division between the realistic (2008-2012) and anachronistic (2013-2014) parts of the model run with the shading in Figure 2, and in all subsequent time series analyses.

In our model the spring bloom is initiated during October (Figure 2a), when the surface chlorophyll concentration averaged over Pine Island Bay first approaches 0.1 mg m^{-3}. Chlorophyll concentration then increases rapidly up to a peak on the order of 1 mg m^{-3}. The timing of this peak in November or December (depending on the year) is early rel-

ative to the observed peak in January [*Arrigo et al.*, 2012]. However the surface (0-10 m) chlorophyll concentration only represents one aspect of the bloom, with timing of the peak generally varying with depth [*Twelves et al.*, 2020]. In some years the initial spring bloom is followed by a distinct later bloom in February and March, likely the result of replenishment of nutrients due to wind-driven mixing [*Castro de la Guardia et al.*, 2019]. There is no clear trend in modelled chlorophyll production over the course of the study period, despite the onset of anachronistic convection across parts of the domain.

The euphotic depth is largely insensitive to the interannual variability in surface chlorophyll concentration (Figure 2b). The minimum of around 40 m consistently occurs in December after a period of rapid shallowing, in line with the initiation of the spring bloom. The subsequent deepening of the euphotic depth is slower, generally remaining within 80 m of the surface until April.

A time series of satellite observations from the GlobColour database (http://hermes.acri.fr, black line in Figure 2b) shows that our model generally performs well in reproducing the magnitude of maximum and minimum euphotic depths. However there is a clear timing bias in the model, with the modelled minimum preceding the satellite data by around one month.

In-situ observations have reported summertime euphotic depths in the polynya area of between 26 m and 40 m [*Park et al.*, 2017], which is shallow compared to our model range (Figure 1 a; see also comparison in Supplementary Figure 1). The strong response of shortwave attenuation to chlorophyll acts as a negative feedback on further phytoplankton growth, [*Manizza et al.*, 2008; *Twelves et al.*, 2020], but here we focus instead on how it impacts physical processes within the Amundsen Sea.

3.2 SST response to chlorophyll

The average summertime SST across Pine Island Bay is elevated by between 0.2 °C and 0.3 °C in *GREEN* compared to *BLUE* (during the realistic period, Figure 3 a), with the strongest anomalies occurring in January. A similar effect is apparent when averaging across the entire Amundsen Sea continental shelf (Figure 3 b), though often peaking in February rather than January.

377 There is strong interannual variability in the magnitude of the anomaly, most visible in

378 the relatively small size of the anomaly in January 2011 compared to the preceding and

379 following years. The sensitivity to chlorophyll reaches almost 0.5 °C in January 2013,

380 but this is during the start of the anachronistic convection period.

3.3 Sea ice response to chlorophyll

382 Sea ice volume, which we plot in Figure 4 using units of effective sea ice thickness (vol-

383 ume per unit ocean area), is modified due to the presence of chlorophyll on the conti-

384 nental shelf. We investigate the seasonality of this response by averaging over 2008-2012

385 separately for the winter (June-July-August) and summer (December-January-February)

386 months.

387 In winter there is a net gain in sea ice volume in $GREEN$ compared to $BLUE$, amount-

388 ing to an increase in effective thickness of 3.5 cm (averaged across the shelf). The largest

389 increases (exceeding 6 cm) are at the western edge of Pine Island Bay and along the front

390 of Getz Ice Shelf.

391 In summer there is a net loss of sea ice volume due to chlorophyll, amounting to a de-

392 crease in effective thickness of 1.7 cm (averaged across the shelf). The largest decreases

393 (exceeding 6 cm) are generally close to the continental shelf break. However there are

394 also areas where the $GREEN$ volume exceeds the $BLUE$ volume even in summer, in-

395 cluding close to the front of Getz Ice Shelf.

3.4 Surface heat balance

397 We consider each of the four components of the air-sea heat flux – shortwave radiation,

398 longwave radiation, sensible heat transfer and latent heat transfer – only for those grid

399 cells where sea ice coverage is below 10%. We choose this threshold – rather than the

400 standard 15% – to reduce the residual contribution of ice to the overall surface heat flux

401 (Supplementary Figure 2).

402 The response of each component to chlorophyll can be considered as the net effect of changes

403 to the flux *per unit area* and changes to the total area A of open water available for heat

404 exchange. To separate out these two processes, we estimate the flux $\mathbb{F}^{scale}$ which would

405 result if the $BLUE$ fluxes were scaled to the $GREEN$ open water area. This is

$$\mathbb{F}_i^{scale} = \mathbb{F}_i^{blue} \frac{A_{green} - A_{blue}}{A_{blue}} \tag{12}$$

for each component i of the heat flux, where $i = LAT, SEN, LW, SW$ and A_{blue}, A_{green} represent the open water area in the $BLUE$ and $GREEN$ experiments respectively. These scaled fluxes are shown as blue filled curves in Figure 5.

The change in shortwave radiative flux is near-identical to the $BLUE$ flux scaled by the change in open-water area (Figure 5 a), as expected given its lack of explicit dependence on sea surface temperature. The annual positive shortwave anomaly is smallest in 2011, a year which also shows a relatively small SST anomaly (Figure 3 b).

The change in longwave radiative flux is of opposite sign to the change in shortwave radiative flux, and almost everywhere constitutes an anomaly leaving the ocean (Figure 5 b). However the anomaly is of smaller amplitude than would be calculated based on the sea ice reduction alone.

The latent heat flux anomaly is negative but, like the shortwave anomaly, almost matches the $BLUE$ flux scaled by the change in open-water area (Figure 5 c). Finally, Figure 5 d shows that the impact of the change in open-water area on sensible heat fluxes is very small, with the flux anomaly instead deriving from the impact of chlorophyll on ocean heating directly.

Taken together, these results suggest that the warm SST anomaly in $GREEN$ is predominantly lost through sensible heat transfer to the atmosphere, whilst the reduction in sea ice cover is responsible for an increase in the integrated shortwave radiative flux incident at the ocean surface and also for an increase in the integrated longwave and latent heat fluxes leaving the ocean. Though the absolute contributions of the changes in longwave, latent and sensible heat fluxes to the overall sea-to-air anomaly are similar, sensible heat flux undergoes by far the largest relative change due to chlorophyll – 17.5%, versus 0.4% and 0.8% for the longwave and latent heat flux anomalies respectively.

3.5 Ocean heat content

Figure 6 a shows the anomalies in ocean heat content, surface heat flux and lateral heat transport as a climatology over the years 2008 - 2012, thus avoiding the period of anachro-

433 nistic convection after 2012. The anomaly in the ocean heat trend $\frac{d}{dt}OHC$ on the con-

434 tinental shelf (defined as the region south of the 1000 m isobath) evolves as

$$\Delta(\frac{d}{dt}OHC) = \Delta\mathbb{F}_{SURF} + \Delta\mathbb{F}_{CONTI} + \Delta\mathbb{F}_{CAV}; \tag{13}$$

435 where $\Delta\mathbb{F}_{CONTI}$ is the anomaly in total lateral heat flux at the continental shelf break,

436 $\Delta\mathbb{F}_{CAV}$ is the anomaly in total lateral heat flux at the front of ice shelf cavities, and $\Delta\mathbb{F}_{SURF}$

437 is the anomaly in surface heat flux. Then, assuming that $\Delta\mathbb{F}_{CAV} \ll \Delta\mathbb{F}_{CONTI}$, we

438 estimate the anomaly in transport of heat onto the continental shelf as the residual

$$\Delta\mathbb{F}_{CONTI} \approx \Delta(\frac{d}{dt}OHC) - \Delta\mathbb{F}_{SURF}. \tag{14}$$

439 The net effect of increased shortwave radiation into the ocean and increased longwave,

440 sensible and latent heat fluxes leaving the ocean is a loss of heat at the sea surface con-

441 tained in the term $\Delta\mathbb{F}_{SURF}$. This anomaly peaks at around 100 EJ yr^{-1} in February,

442 but the surface heat loss is partially counteracted by a net gain in heat through trans-

443 port of around 50 EJ yr^{-1}.

444 During winter the anomaly in lateral heat transport is negligible. There is now a net gain

445 of heat at the sea surface, which drives a net increase in the ocean heat trend peaking

446 at just over 50 EJ yr^{-1} in May.

447 In Figure 6 b we show a schematic representing the integration of these trends over the

448 calendar year. The yearly changes are small compared to the seasonal changes shown

449 in Figure 6 a, but there is a robust signal of excess ocean cooling due to chlorophyll.

450 The impact of increased incoming shortwave and increased outgoing longwave, latent and

451 sensible heat fluxes is an outgoing $(GREEN-BLUE)$ anomaly of 19.8 EJ yr^{-1} from

452 the open water portions of the Amundsen Sea continental shelf. In contrast, those ar-

453 eas covered by sea ice are subject to a net incoming anomaly of 14.9 EJ yr^{-1}. We do not

454 attempt to diagnose the contributions to this latter anomaly; however, we note that in-

455 creased ice production in winter releases more latent heat to the sea surface, likely con-

456 tributing to $\Delta\mathbb{F}_{SICE}$.

457 Overall the presence of chlorophyll boosts Amundsen Sea surface heat loss by 4.9 EJ yr^{-1}.

458 This is complemented by a net heat export anomaly of 1.9 EJ yr^{-1} leaving the conti-

nental shelf, producing an overall ocean cooling anomaly of 6.8 EJ yr^{-1} due to chloro-
phyll.

3.6 Impact on AASW and near-surface melt rates

The increased near-surface warming in the $GREEN$ experiment drives changes to the
AASW layer, defined here as the water mass lying on the continental shelf with temper-
ature greater than 0 °C and salinity less than 34 g kg^{-1} (Figure 7 a). In both experi-
ments there is strong seasonality, but $GREEN$ consistently shows a slightly greater vol-
ume of AASW.

The near-surface melt rate, defined here as the meltwater flux originating from shallower
than 50 m on the ice shelf, shows strong interannual variability correlating with the vol-
ume of AASW. With more warm water close to the surface due to shortwave attenua-
tion by chlorophyll, the shallowest portions of the ice shelves undergo stronger melting
in $GREEN$ compared to $BLUE$ (Figure 7 b). This strengthening is small in most years,
but in early 2010 the peak near-surface melt rate is increased by over 20% due to chloro-
phyll.

3.7 Impact on CDW and ice shelf melt rates at depth

Meanwhile the CDW layer, defined here as the water mass lying on the continental shelf
with temperature greater than 0 °C and salinity greater than 34.5 g kg^{-1}, is relatively
stable seasonally, but shows signs of the decadal variability seen in observations [*Dutrieux
et al.*, 2014], as well as the anachronistic convection after 2012 reported by *Naughten et al.*
[2023]. The volume of CDW is consistently less within $GREEN$ compared to $BLUE$,
but there is an increasing divergence between the time series over the study period (Fig-
ure 8 a).

The time evolution of the total ice shelf meltwater flux (below 50 m) resembles that of
the CDW volume, both in the trend and in the anomaly caused by chlorophyll (Figure
8 b). The reduction in CDW on the continental shelf corresponds to a reduction in the
heat ultimately available for basal melting. However whereas there is a clear divergence
in the time series for CDW volume, the difference in melt rate remains on the order of
40 Gt yr^{-1} over the same period.

488 The majority of the anomaly between the two experiments comes from a chlorophyll-

489 forced reduction in melt from ice lying between 200 m and 500 m depth (Figure 8 c). This

490 is the same depth range where *Naughten et al.* [2023] report the greatest sensitivity of

491 future Amundsen Sea melt rates to global emission scenarios. Integrating over all depths

492 for the realistic period (2008-2012), the impact of chlorophyll is a reduction in melt rate

493 of just under 7%, from 510 Gt yr^{-1} to 476 Gt yr^{-1}.

3.8 Impact of chlorophyll during anachronistic convection periods

495 The model undergoes periods of convection in both the $GREEN$ and $BLUE$ experiments,

496 as it does with a Jerlov water-type scheme [*Naughten et al.*, 2022]. Figure 9 focuses on

497 Pine Island Bay, where the onset of convection has a drastic effect on water mass struc-

498 ture (see also Figure 1 b). While the convection may somewhat affect the model's ap-

499 plicability to the Amundsen Sea for this period, from the point of view of our process

500 study it provides an opportunity to examine bio-optical feedbacks in a slightly different

501 regime, one which may be applicable outside the region. We reiterate that this aspect

502 of our analysis is not applicable to the actual conditions prevailing in the Amundsen re-

503 gion between 2008 and 2014.

504 Although the timing of the convection onset is the same for both experiments, the mag-

505 nitude of the cooling is greater in $GREEN$ than in $BLUE$ (Figure 9 a). Furthermore,

506 the anomaly between the two experiments is substantially greater than that prior to the

507 onset of anachronistic convection in 2012.

508 The convective cooling of the deepest waters translates into a decrease in the volume of

509 Circumpolar Deep Water (CDW) circulating around Pine Island Bay (Figure 9 b). Again,

510 the $GREEN$ - $BLUE$ anomaly during anachronistic convection is substantially greater

511 than that during the realistic warm phase. Whereas in $BLUE$ there remains a CDW vol-

512 ume of around 1.1 x 10^4 km^3 in December 2014, in $GREEN$ this is reduced to around

513 3000 km^3.

514 In turn the ice shelves fringing Pine Island Bay, which respond only very weakly to chloro-

515 phyll before 2012, becomes highly sensitive to chlorophyll after 2012 (Figure 9 c). Dur-

516 ing 2014 the total melt within the $GREEN$ experiment is approximately half that from

517 the $BLUE$ experiment. Whilst these results do not relate to expected conditions under-

518 neath Pine Island Glacier, they may be relevant to those parts of the Antarctic conti-

519 nental shelf outside the Amundsen Sea where CDW intrusions are weak.

4 Discussion

4.1 Sensitivity of polynyas to chlorophyll

522 In spring the retreat of sea ice in the Amundsen Sea and the re-emergence of polynyas

523 leaves phytoplankton exposed to solar radiation. This causes phytoplankton to bloom

524 and saturate the upper ocean with highly attenuating chlorophyll. Our setup of MIT-

525 gcm simulates this sea ice retreat, whilst BLING reproduces the seasonal increases both

526 in chlorophyll and in light attenuation. As more heat from the sun is trapped close to

527 the surface there are changes to the polynya heat balance, which our changes to the MITgcm-

528 BLING code allow us to evaluate for the first time.

529 Modelled chlorophyll concentrations in Pine Island Bay of around 1 mg m^{-3} stimulate

530 between 0.2°C and 0.3°C of additional warming on top of that which would result from

531 attenuation by water molecules alone. Hence our results indicate that phytoplankton blooms

532 play a substantial role in determining the summertime sea surface temperature in polynyas.

533 The anomaly is on the same order of magnitude as that reported when *Manizza et al.*

534 [2005] originally implemented attenuation by chlorophyll in a global ocean model, and

535 is in line with previous studies which showed that biologically mediated changes in SST

536 could influence marine heatwaves and storm tracks [*Gnanadesikan et al.*, 2010, 2019].

537 Attenuation by chlorophyll enhances the magnitude of the seasonal sea ice cycle, via thicker

538 winter ice and thinner summertime ice, as originally observed in modelling on a global

539 domain by *Manizza et al.* [2005]. Ice effective thickness responds more weakly to chloro-

540 phyll in summer, whilst in winter it increases substantially. Though these changes are

541 small overall relative to the interannual variability in sea ice cover, they represent a po-

542 tential feedback mechanism, since it is the initial retreat of sea ice which itself stimulates,

543 via biological production, the increase in near-surface heat attenuation.

544 *Pefanis et al.* [2020] found that light attenuation by CDOM caused a net summertime

545 heat loss to the atmosphere across most of the Arctic in their model, but a net summer-

546 time heat gain close to the sea ice edge. They attribute the latter to reduced sea ice cover

547 at the edge of the ice pack. We find that attenuation by chlorophyll generates similarly

548 divergent effects in the Amundsen Sea, but we go further in separating the terms con-

tributing to this anomaly in polynyas. Reduced sea ice cover opens up more of the ocean surface to shortwave and longwave radiation, but in the latter case the additional heat generated is outweighed by the heat lost by an increase in longwave radiation leaving the ocean. There is also an increase in latent heat loss, which scales with the increase in open water area, while the increases in sensible heat loss are instead largely driven by the warmer sea surface. Overall, there is a net heat loss in open water areas (ice cover less than 10%) and a net heat gain in areas with ice cover (greater than 10%). Whilst *Pefanis et al.* [2020] ascribe the regions of heat gain in their simulations purely to reduced ice cover, our results suggest that chlorophyll may also lead to surface heat gain via increased wintertime sea ice growth and the associated release of latent heat at the sea surface.

As in previous modelling with BLING in the Amundsen Sea [*Twelves et al.*, 2020], the simulated phytoplankton bloom is early relative to the observed bloom. In our case that means that by January the bloom is already in decline. Two effects of this bias could be imagined. On the one hand there is less chlorophyll to attenuate light when that attenuation would contribute most strongly to the heat budget. Conversely, the early bloom allows more time for the springtime surface warming to equilibrate with the atmosphere, which potentially exaggerates the impact of the SST anomaly on heat loss to the atmosphere and minimises the impact of the SST anomaly on sea ice.

Our work represents an initial attempt to quantify the impact of chlorophyll on polynya thermodynamics. In the future the values of the coefficients linking chlorophyll concentration to light attenuation should be constrained specifically for the mixture of diatoms and *P. antarctica* found in the Amundsen Sea [*Lee et al.*, 2022], utilizing a combination of in-situ and satellite observations. Ultimately, the use of a coupled ocean-atmosphere model would be necessary to accurately represent turbulent heat fluxes at the polynya surface.

4.2 Sensitivity of ice shelves to chlorophyll

In our study we consider only chlorophyll and thus exclude CDOM from our analysis. This can be justified based on the dominant role that chlorophyll plays in ocean colour in the Southern Ocean overall [*Dutkiewicz et al.*, 2015], but also on the especially high chlorophyll concentrations that are driven by iron fluxes from ice shelves in the Amund-

sen Sea. However recent work by *Son et al.* [2023] found spatially variable CDOM concentrations in the Amundsen Sea, whilst particulate matter from ice shelves themselves may also contribute substantially to light attenuation.

Nonetheless our results indicate that chlorophyll plays a small but non-negligible role in modulating the quantity of warm and saline CDW present on the Amundsen Sea continental shelf. Over the simulation period, chlorophyll boosts heat loss to the atmosphere, cools the ocean, and leads to a decrease in the volume of CDW. With less warm and salty water at depth, basal melting is consistently - though weakly - reduced over the study period. Chlorophyll does not impact the shape of the melt rate distribution with respect to depth, and thus the greatest sensitivity is over the 200-500 m depth range where the bulk of basal melting occurs. This is also the same depth range where *Naughten et al.* [2023] showed that future melt rates are most sensitive to future emission scenario (their extended data Figure 8).

The overall melt rate trend in our results – and in the real Amundsen Sea – is driven by intrusions of modified Circumpolar Deep Water (CDW), which is in turn dominated by processes at the continental shelf break [*Kimura et al.*, 2017]. The years covered in our study form part of a period of decadal-scale cooling – with associated reductions in melt rate – on the Amundsen Sea continental shelf. On top of this trend, our model captures a small seasonal component relating to melting close to the sea surface. Here, within the upper 50 m of ice shelves, melt rates are driven by AASW and, since the AASW layer expands in response to chlorophyll, the net effect of chlorophyll is an increase in melt rates. This melting close to the front of ice shelves due to summertime heating of the surface ocean has been seen in some previous Amundsen Sea modelling [*Twelves et al.*, 2020], but is little studied precisely because it is much smaller in magnitude than the basal melting that occurs at depth.

Jacobs et al. [1992] introduced the partition of ice shelf melting between three distinct modes. Mode I melting occurs when dense shelf water, mixed downward from the surface, is pushed to a depth where its temperature exceeds the in-situ melting point. Mode II melting occurs when already warm and saline CDW moves onto the continental shelf and floods ice shelf cavities, whilst Mode III melting occurs when the ocean surface is warmed seasonally and then moves beneath the ice shelf front. Using this terminology, the Amundsen Sea is heavily dominated by Mode II melting, with a much smaller con-

tribution from Mode III. Mode I melting does not currently occur on the Amundsen Sea shelf, though it may have in the past, and may occur in our model during anachronistic convection periods. We see in our results that when anachronistic convection does occur, the impact of chlorophyll on melt rates is far greater, and so we suggest similar studies should be conducted in those locations, such as the Weddell Sea, where Mode I melting is thought to take place.

Recently *Stewart et al.* [2019] showed that melting beneath Ross Ice Shelf is to a large extent driven by solar radiation absorbed in the adjacent polynya. This Mode III melting occurs adjacent to a relatively large phytoplankton bloom affecting ocean colour [*Arrigo and Van Dijken*, 2003]. Based on our results, we expect that this bloom modulates AASW content in the Ross Sea polynya and thus affects the transfer of solar heating to the ice shelf. The expanded coverage of biogeochemical Argo floats to the Ross Sea continental shelf [under the SOCCOM program, *Sarmiento et al.*, 2023] will provide physical and biogeochemical datasets that could complement future modelling in this direction. Meanwhile in East Antarctica *Herraiz-Borreguero et al.* [2016], have shown that Mode III melting can drive large iron fluxes from the Amery Ice Shelf to Prydz Bay. This raises the prospect of a two-way coupling between phytoplankton blooms and iron supply in the region; whereby ice shelves supply iron to the phytoplankton bloom, but the bloom itself affects the flux of iron leaving the ice shelf cavity.

5 Conclusion

In this study we have demonstrated, for the first time, that the same phytoplankton blooms that rely on nearby ice shelves for supply of nutrients (most especially iron) can themselves affect the supply of oceanic heat that drives basal melting. The production of chlorophyll in the spring bloom strengthens the attenuation of shortwave radiation in the visible wavelengths, so that more solar energy is dissipated close to the polynya surface. Here this heat is more easily lost to the atmosphere in longwave, sensible and latent heat fluxes. Meanwhile the reduced solar radiation below the surface layers leaves deeper waters cooler than they would be in the absence of phytoplankton. As this cooler layer interacts with Circumpolar Deep Water below, the bio-optical feedback ultimately results in a reduction of around 7% in rates of melting from Amundsen Sea ice shelves than would be the case in the complete absence of chlorophyll.

Here we examine the thermodynamic impact of chlorophyll only in the Amundsen Sea, a region characterized by latent heat-dominated polynyas and Mode II-dominated ice shelves. However by extending our analysis to years where the model shows convection not seen in observations, we infer that chlorophyll likely has a stronger impact on ice shelf melting at those locations where Mode II does not dominate. Similarly, whilst our model results show moderate impacts of chlorophyll on SST and sea ice in latent heat polynyas, it is likely that biologically productive sensible heat polynyas – formed by the upwelling of warmer water from depth [*Prend et al.*, 2019] – would be more sensitive to chlorophyll, given their purely thermodynamic origin. At present, it is challenging to investigate the bio-optical feedback with observations, and thus further numerical modelling is merited to investigate this mechanism both in the Amundsen Sea and on the broader Southern Ocean scale.

References

Alderkamp, A.-C., et al., Iron from melting glaciers fuels phytoplankton blooms in the amundsen sea (southern ocean): Phytoplankton characteristics and productivity, *Deep Sea Research Part II: Topical Studies in Oceanography*, *71*, 32–48, 2012.

Arneborg, L., A. Wåhlin, G. Björk, B. Liljebladh, and A. Orsi, Persistent inflow of warm water onto the central amundsen shelf, *Nature Geoscience*, *5*(12), 876–880, 2012.

Arrigo, K. R., and G. L. Van Dijken, Phytoplankton dynamics within 37 antarctic coastal polynya systems, *Journal of Geophysical Research: Oceans*, *108*(C8), 2003.

Arrigo, K. R., K. E. Lowry, and G. L. van Dijken, Annual changes in sea ice and phytoplankton in polynyas of the amundsen sea, antarctica, *Deep Sea Research Part II: Topical Studies in Oceanography*, *71*, 5–15, 2012.

Arrigo, K. R., G. L. van Dijken, and A. L. Strong, Environmental controls of marine productivity hot spots around antarctica, *Journal of Geophysical Research: Oceans*, *120*(8), 5545–5565, doi:10.1002/2015JC010888, 2015.

Assmann, K., A. Jenkins, D. Shoosmith, D. Walker, S. Jacobs, and K. Nicholls, Variability of circumpolar deep water transport onto the amundsen sea continental shelf through a shelf break trough, *Journal of Geophysical Research: Oceans*, *118*(12), 6603–6620, 2013.

Bai, Y., L. Zhao, J. Xiao, and S. Lin, Contraction and warming of antarctic bottom water in the amundsen sea, *Acta Oceanologica Sinica*, *41*(4), 68–79, 2022.

Bett, D. T., P. R. Holland, A. C. Naveira Garabato, A. Jenkins, P. Dutrieux, S. Kimura, and A. Fleming, The impact of the amundsen sea freshwater balance on ocean melting of the west antarctic ice sheet, *Journal of Geophysical Research: Oceans*, *125*(9), e2020JC016,305, 2020.

Bryan, F., B. Kauffman, W. Large, and P. Gent, Ncar csm flux coupler. technical note, *Tech. rep.*, National Center for Atmospheric Research, Boulder, CO (United States . . . , 1996.

Cahill, B. E., P. Kowalczuk, L. Kritten, U. Gräwe, J. Wilkin, and J. Fischer, Estimating the seasonal impact of optically significant water constituents on surface heating rates in the western baltic sea, *Biogeosciences*, *20*(13), 2743–2768, 2023.

Castro de la Guardia, L., Y. Garcia-Quintana, M. Claret, X. Hu, E. Galbraith, and P. G. Myers, Assessing the role of high-frequency winds and sea ice loss on arctic phytoplankton blooms in an ice-ocean-biogeochemical model, *Journal of Geophysical Research: Biogeosciences*, *124*(9), 2728–2750, 2019.

Christie, F. D., R. G. Bingham, N. Gourmelen, S. F. Tett, and A. Muto, Four-decade record of pervasive grounding line retreat along the bellingshausen margin of west antarctica, *Geophysical Research Letters*, *43*(11), 5741–5749, 2016.

Dinniman, M. S., P. St-Laurent, K. R. Arrigo, E. E. Hofmann, and G. L. van Dijken, Analysis of iron sources in antarctic continental shelf waters, *Journal of Geophysical Research: Oceans*, *125*(5), e2019JC015,736, 2020.

Dutkiewicz, S., A. Hickman, O. Jahn, W. Gregg, C. Mouw, and M. Follows, Capturing optically important constituents and properties in a marine biogeochemical and ecosystem model, *Biogeosciences*, *12*(14), 4447–4481, 2015.

Dutrieux, P., et al., Strong sensitivity of pine island ice-shelf melting to climatic variability, *Science*, *343*(6167), 174–178, 2014.

Galbraith, E. D., A. Gnanadesikan, J. P. Dunne, and M. R. Hiscock, Regional impacts of iron-light colimitation in a global biogeochemical model, *Biogeosciences*, *7*(3), 1043–1064, 2010.

Gerringa, L. J., A.-C. Alderkamp, P. Laan, C.-E. Thuroczy, H. J. De Baar, M. M. Mills, G. L. van Dijken, H. van Haren, and K. R. Arrigo, Iron from melting glaciers fuels the phytoplankton blooms in amundsen sea (southern ocean): Iron

biogeochemistry, *Deep Sea Research Part II: Topical Studies in Oceanography*, *71*, 16–31, 2012.

Gnanadesikan, A., K. Emanuel, G. A. Vecchi, W. G. Anderson, and R. Hallberg, How ocean color can steer pacific tropical cyclones, *Geophysical Research Letters*, *37*(18), 2010.

Gnanadesikan, A., G. E. Kim, and M.-A. S. Pradal, Impact of colored dissolved materials on the annual cycle of sea surface temperature: Potential implications for extreme ocean temperatures, *Geophysical Research Letters*, *46*(2), 861–869, 2019.

Goldberg, D. N., A. G. Twelves, P. R. Holland, and M. G. Wearing, The non-local impacts of antarctic subglacial runoff, *Journal of Geophysical Research: Oceans*, *128*(10), e2023JC019,823, 2023.

Gourmelen, N., et al., Channelized melting drives thinning under a rapidly melting antarctic ice shelf, *Geophysical Research Letters*, *44*(19), 9796–9804, 2017.

Hernandez, O., J. Jouanno, V. Echevin, and O. Aumont, Modification of sea surface temperature by chlorophyll concentration in the atlantic upwelling systems, *Journal of Geophysical Research: Oceans*, *122*(7), 5367–5389, 2017.

Herraiz-Borreguero, L., D. Lannuzel, P. Van Der Merwe, A. Treverrow, and J. Pedro, Large flux of iron from the amery ice shelf marine ice to prydz bay, east antarctica, *Journal of Geophysical Research: Oceans*, *121*(8), 6009–6020, 2016.

Hersbach, H., et al., The era5 global reanalysis, *Quarterly Journal of the Royal Meteorological Society*, *146*(730), 1999–2049, 2020.

Jacobs, S., H. Helmer, C. Doake, A. Jenkins, and R. Frolich, Melting of ice shelves and the mass balance of antarctica, *Journal of Glaciology*, *38*(130), 375–387, 1992.

Jerlov, N. G., *Marine optics*, Elsevier, 1976.

Kimura, S., et al., Oceanographic controls on the variability of ice-shelf basal melting and circulation of glacial meltwater in the amundsen sea embayment, antarctica, *Journal of Geophysical Research: Oceans*, *122*(12), 10,131–10,155, 2017.

Large, W. G., J. C. McWilliams, and S. C. Doney, Oceanic vertical mixing: A review and a model with a nonlocal boundary layer parameterization, *Reviews of Geophysics*, *32*(4), 363–403, 1994.

Lee, Y., J. Park, J. Jung, and T. W. Kim, Unprecedented differences in phytoplankton community structures in the amundsen sea polynyas, west antarctica, *Environmental Research Letters*, *17*(11), 114,022, 2022.

Locarnini, M., et al., World ocean atlas 2018, volume 1: Temperature, 2018.

Losch, M., Modeling ice shelf cavities in az coordinate ocean general circulation model, *Journal of Geophysical Research: Oceans*, *113*(C8), 2008.

Losch, M., D. Menemenlis, J.-M. Campin, P. Heimbach, and C. Hill, On the formulation of sea-ice models. part 1: Effects of different solver implementations and parameterizations, *Ocean Modelling*, *33*(1-2), 129–144, 2010.

Manizza, M., C. Le Quéré, A. J. Watson, and E. T. Buitenhuis, Bio-optical feedbacks among phytoplankton, upper ocean physics and sea-ice in a global model, *Geophysical Research Letters*, *32*(5), 2005.

Manizza, M., C. Le Quéré, A. J. Watson, and E. T. Buitenhuis, Ocean biogeochemical response to phytoplankton-light feedback in a global model, *Journal of Geophysical Research: Oceans*, *113*(C10), 2008.

Marshall, J., C. Hill, L. Perelman, and A. Adcroft, Hydrostatic, quasi-hydrostatic, and nonhydrostatic ocean modeling, *Journal of Geophysical Research: Oceans*, *102*(C3), 5733–5752, 1997.

Morlighem, M., et al., Deep glacial troughs and stabilizing ridges unveiled beneath the margins of the antarctic ice sheet, *Nature Geoscience*, *13*(2), 132–137, 2020.

Naughten, K. A., P. R. Holland, P. Dutrieux, S. Kimura, D. T. Bett, and A. Jenkins, Simulated twentieth-century ocean warming in the amundsen sea, west antarctica, *Geophysical Research Letters*, *49*(5), e2021GL094,566, 2022.

Naughten, K. A., P. R. Holland, and J. De Rydt, Unavoidable future increase in west antarctic ice-shelf melting over the twenty-first century, *Nature Climate Change*, pp. 1–7, 2023.

Nissen, C., and M. Vogt, Factors controlling the competition between *Phaeocystis* and diatoms in the southern ocean and implications for carbon export fluxes, *Biogeosciences*, *18*(1), 251–283, doi:10.5194/bg-18-251-2021, 2021.

Oliver, H., P. St-Laurent, R. M. Sherrell, and P. L. Yager, Modeling iron and light controls on the summer phaeocystis antarctica bloom in the amundsen sea polynya, *Global Biogeochemical Cycles*, *33*(5), 570–596, doi:10.1029/2018GB006168, 2019.

Park, J., F. I. Kuzminov, B. Bailleul, E. J. Yang, S. Lee, P. G. Falkowski, and M. Y. Gorbunov, Light availability rather than fe controls the magnitude of massive phytoplankton bloom in the amundsen sea polynyas, antarctica, *Limnology and*

774   *Oceanography, 62*(5), 2260–2276, doi:10.1002/lno.10565, 2017.

775   Pefanis, V., S. N. Losa, M. Losch, M. A. Janout, and A. Bracher, Amplified arc-

776   tic surface warming and sea ice loss due to phytoplankton and colored dissolved

777   material, *Geophysical Research Letters, 47*(21), e2020GL088,795, 2020.

778   Prend, C. J., S. T. Gille, L. D. Talley, B. G. Mitchell, I. Rosso, and M. R. Mazloff,

779   Physical drivers of phytoplankton bloom initiation in the southern ocean's scotia

780   sea, *Journal of Geophysical Research: Oceans, 124*(8), 5811–5826, 2019.

781   Sarmiento, J. L., et al., The southern ocean carbon and climate observations and

782   modeling (soccom) project: A review, *Progress in Oceanography*, p. 103130, 2023.

783   Shean, D. E., I. R. Joughin, P. Dutrieux, B. E. Smith, and E. Berthier, Ice shelf

784   basal melt rates from a high-resolution digital elevation model (dem) record for

785   pine island glacier, antarctica, *The Cryosphere, 13*(10), 2633–2656, 2019.

786   Shepherd, A., et al., Trends in antarctic ice sheet elevation and mass, *Geophysical*

787   *Research Letters, 46*(14), 8174–8183, 2019.

788   Son, J., J. Jung, Y. Lee, T.-W. Kim, J. Park, M. H. Jeon, and M. O. Park, Con-

789   trasting optical properties of dissolved organic matter between oceanic regions

790   near the getz and dotson ice shelves in the amundsen sea, west antarctica, *Marine*

791   *Chemistry*, p. 104335, 2023.

792   St-Laurent, P., P. L. Yager, R. M. Sherrell, S. E. Stammerjohn, and M. S. Din-

793   niman, Pathways and supply of dissolved iron in the amundsen sea (antarc-

794   tica), *Journal of Geophysical Research: Oceans, 122*(9), 7135–7162, doi:

795   10.1002/2017JC013162, 2017.

796   St-Laurent, P., P. L. Yager, R. M. Sherrell, H. Oliver, M. S. Dinniman, and S. E.

797   Stammerjohn, Modelling the seasonal cycle of iron and carbon fluxes in the

798   amundsen sea polynya, antarctica, *Journal of Geophysical Research: Oceans,*

799   *124*(3), 1544–1565, doi:10.1029/2018JC014773, 2019.

800   Stewart, C. L., P. Christoffersen, K. W. Nicholls, M. J. Williams, and J. A.

801   Dowdeswell, Basal melting of ross ice shelf from solar heat absorption in an ice-

802   front polynya, *Nature Geoscience, 12*(6), 435, 2019.

803   Tamsitt, V., L. D. Talley, M. R. Mazloff, and I. Cerovečki, Zonal variations in the

804   southern ocean heat budget, *Journal of Climate, 29*(18), 6563–6579, 2016.

805   Twelves, A. G., D. N. Goldberg, S. F. Henley, M. Mazloff, and D. Jones, Self-

806   shading and meltwater spreading control the transition from light to iron limi-

807   tation in an antarctic coastal polynya, *Journal of Geophysical Research: Oceans*,

808   p. e2020JC016636, 2020.

809 Verdy, A., and M. R. Mazloff, A data assimilating model for estimating southern

810   ocean biogeochemistry, *Journal of Geophysical Research: Oceans*, *122*(9), 6968–

811   6988, doi:10.1002/2016JC012650, 2017.

812 Yager, P. L., R. Sherrell, R. Sipler, et al., A carbon budget for the amundsen sea

813   polynya, antarctica: Estimating net community production and export in a highly

814   productive polar ecosystem, *Elementa-Science Of The Anthropocene*, *4*(140), 2016.

815 Yu, X., Z. Lee, S. Shang, M. Wang, and L. Jiang, Estimating the water-leaving

816   albedo from ocean color, *Remote Sensing of Environment*, *269*, 112,807, 2022.

817 Zheng, Y., K. J. Heywood, B. G. Webber, D. P. Stevens, L. C. Biddle, L. Boehme,

818   and B. Loose, Winter seal-based observations reveal glacial meltwater surfacing

819   in the southeastern amundsen sea, *Communications Earth & Environment*, *2*(1),

820   1–9, 2021.

821 Zweng, M., et al., World ocean atlas 2018, volume 2: Salinity, 2019.

Acknowledgements

Open Research

MITgcm code can be accessed publicly at `mitgcm.org`, and the MITgcm manual is avail-
able at `https://doi.org/10.5281/zenodo.1409237`. B-SOSE outputs are available at
`http://sose.ucsd.edu/bsose\_solution\_Iter105.html`. The modified code coupling
biology and physics is available at `https://github.com/atwelves/MITgcm/tree/master;`

data used to plot figures in this manuscript are also available at the open-access repository `10.5281/zenodo.10830064`. The scripts needed to reproduce figures from the output are archived at `https://github.com/atwelves/Chlorophyll-production-in-the-Amundsen-Sea`. GlobColour data (`http://globcolour.info`) used in this study has been developed, validated, and distributed by ACRI-ST, France.

Acronyms

DIS Dotson Ice Shelf

PIIS Pine Island Ice Shelf

PIP Pine Island Polynya

ASP Amundsen Sea Polynya

PIB Pine Island Bay

NPP Net Primary Production

NCP Net Community Production

CDW Circumpolar Deep Water

WW Winter Water

AASW Antarctic Surface Water

BLING Biology Light Iron Nutrients Gases model

B-SOSE Biogeochemical Southern Ocean State Estimation

MITgcm Massachusetts Institute of Technology general circulation model

KPP K-Profile Parameterization of vertical mixing
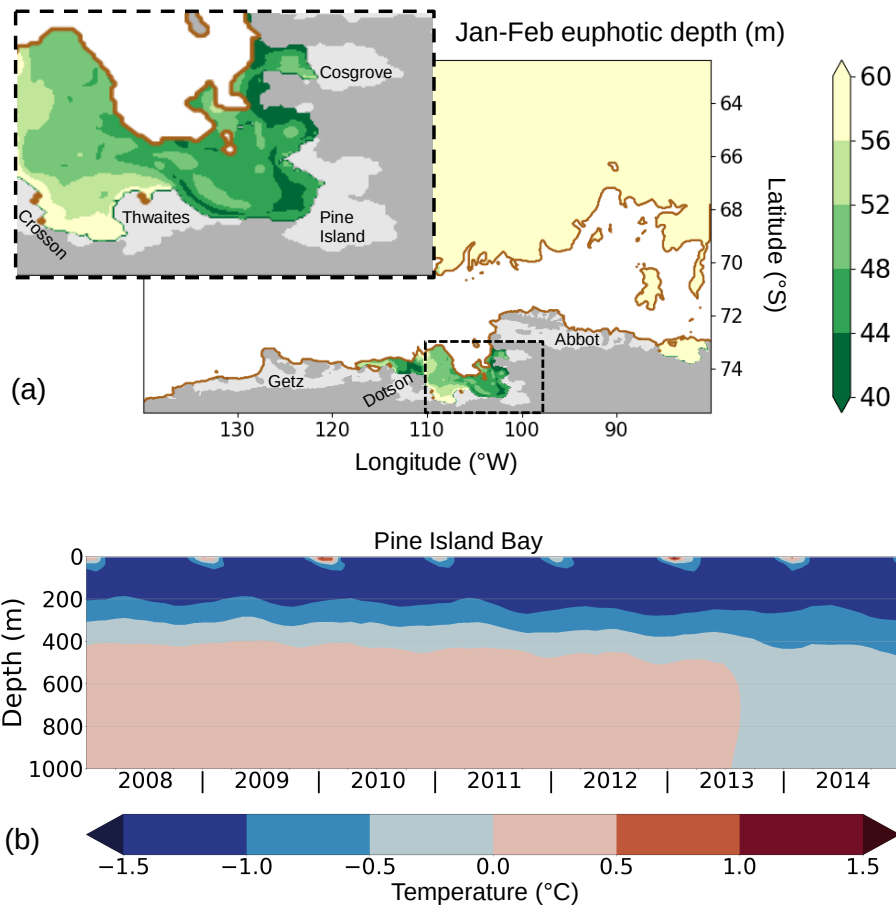
Figure 1. (a) The model domain covers the entire Amundsen Sea and includes the seven ice shelves labeled, plus two major polynyas. The inset is a closeup view of the area enclosed by the dashed line, covering Pine Island Bay. The boundary of the continental shelf approximately follows a 1000 m isobath. The colourmap shows the modelled springtime euphotic depth in open-water areas, averaged over January and February across the entire model run. The sea ice coverage (concentration >15%) is shown in white. (b) Evolution of the vertical structure in temperature within the Pine Island Bay sub-domain, showing the onset of convection during 2013.
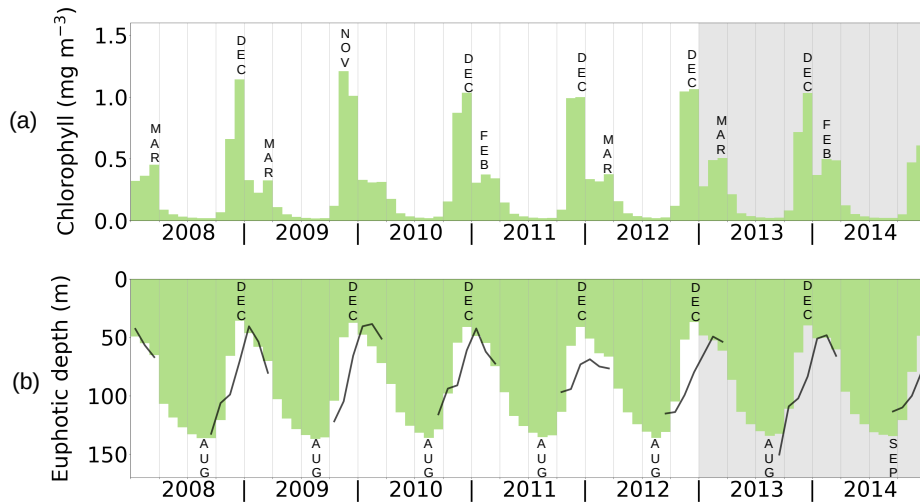
Figure 2. Quantities averaged over the Pine Island Bay region shown in Figure 1. The variation in chlorophyll in (a) is strongly seasonal, as is the the euphotic depth plotted in (b). The month where the spring bloom peaks is marked in each case, as is the peak of the late summer bloom (where present). The black line in (b) shows the euphotic depth derived by GlobColour based on satellite observations. Grey shading marks the period of anachronistic convection.
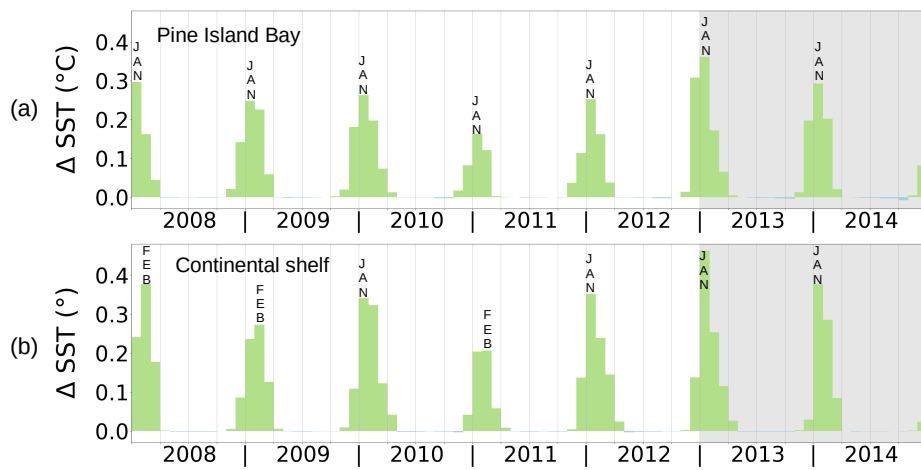
Figure 3. The anomaly in sea surface temperature due to chlorophyll, plotted for Pine Island Bay (a) and for the continental shelf as a whole (b). The month where the greatest anomaly occurs is marked in each case. Grey shading marks the period of anachronistic convection.
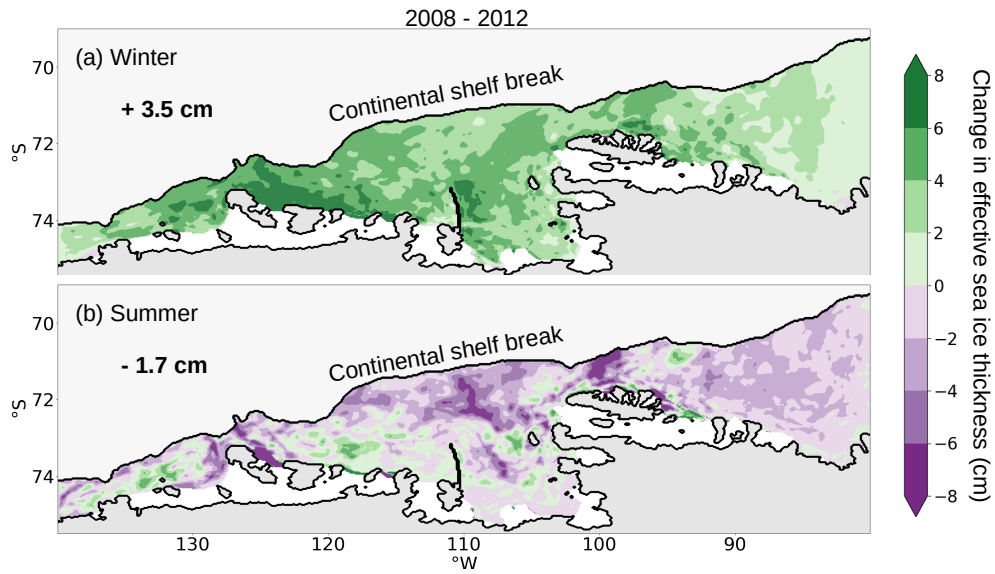
Figure 4. Impact of chlorophyll on wintertime (a) and summertime (b) effective sea ice thickness, i.e. volume per area, averaging across months June to August in the former and across months December to February in the latter case. Also stated are the anomalies averaged across the continental shelf.
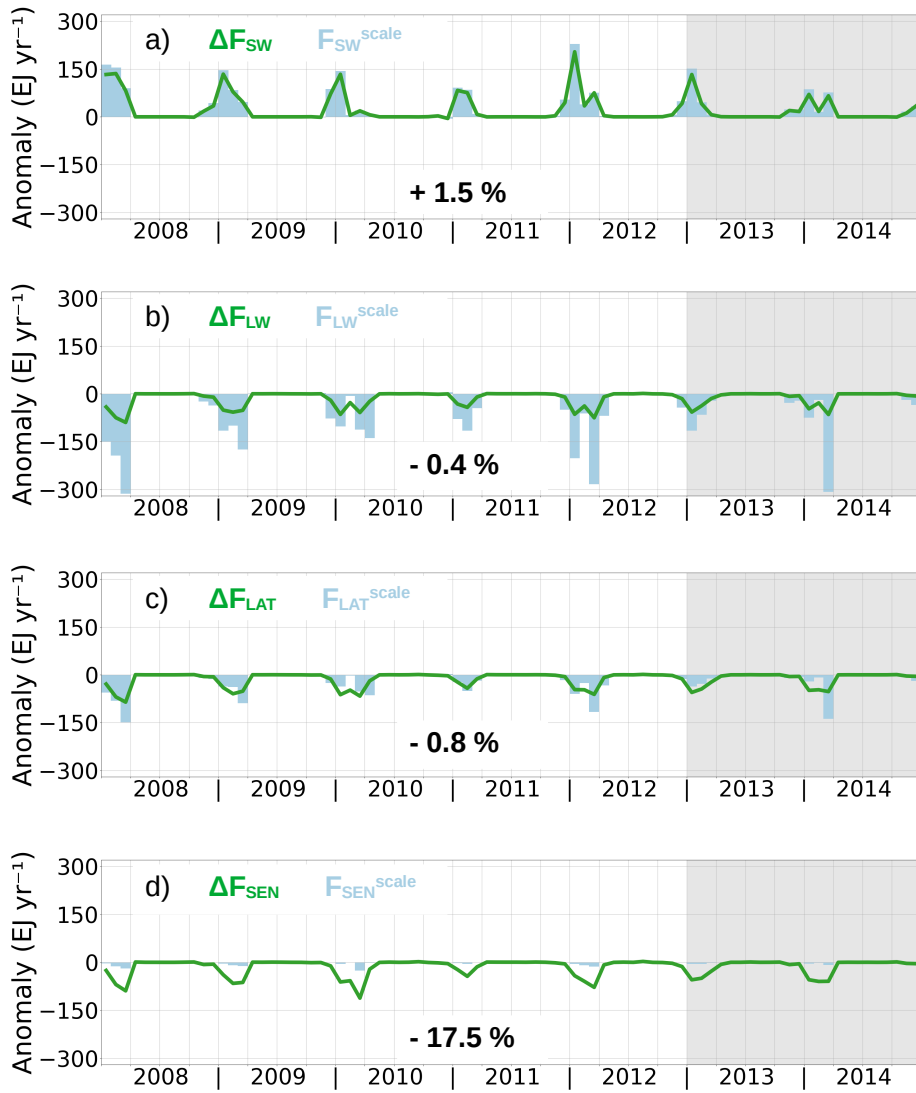
Figure 5. Air-sea heat flux anomalies due to chlorophyll, integrated over the entire Amundsen Sea continental shelf, excluding ice shelf cavities. Positive values indicate that $GREEN$ has a greater heat flux into the ocean than $BLUE$. The overall surface heat flux in open water areas (sea ice cover less than 10%) is composed of contributions from shortwave radiation (a), longwave radiation (b), sensible heat transfer (c) and latent heat transfer (d). In each case the solid green line shows the $GREEN$ - $BLUE$ anomaly, whilst the blue shading shows the $BLUE$ field scaled by the percentage change in sea ice cover $(GREEN$ - $BLUE)/BLUE$. The percentage change in each component between 2008 and 2012 is stated in bold on each plot. Grey shading marks the period of anachronistic convection.
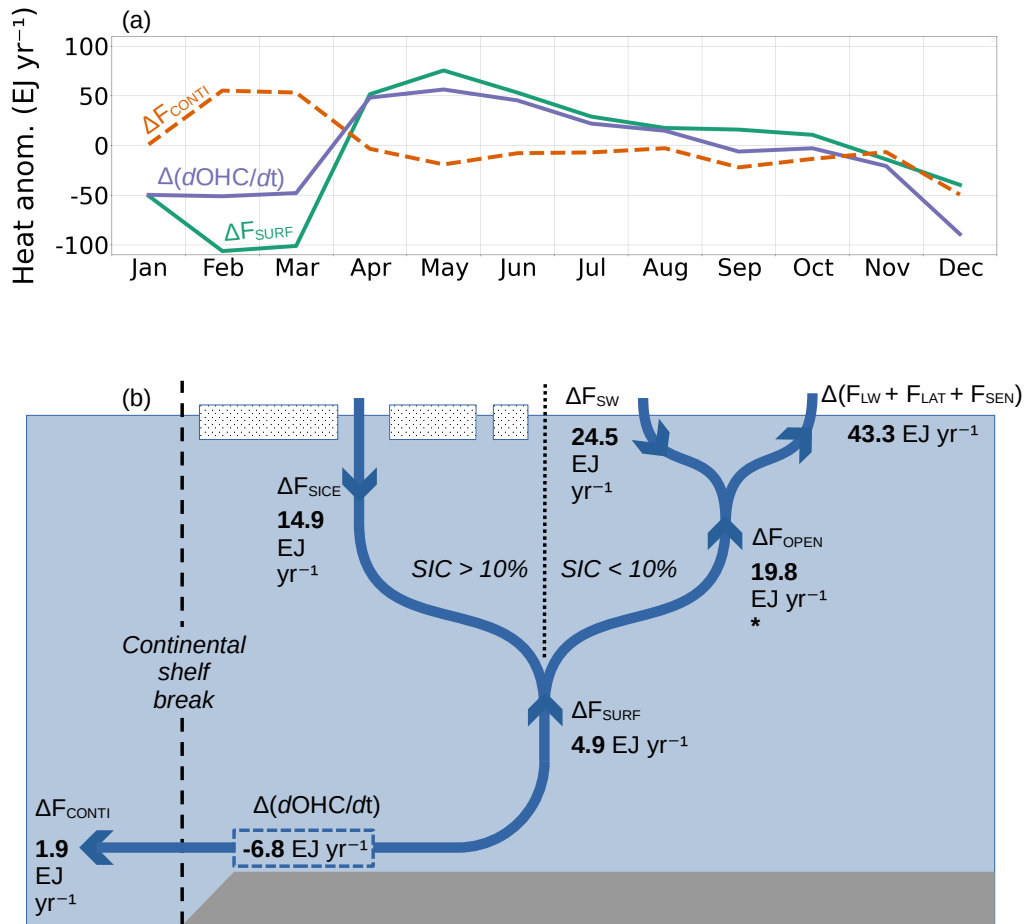
Figure 6. (a) Impact of chlorophyll on surface heat flux (green solid line), overall heat trend (purple line) and lateral heat transport calculated as a residual (orange dashed line), averaged across 2008-2012. (b) Schematic of heat flux anomalies induced by chlorophyll, with values calculated by integrating model outputs from 2008-2012. The dashed line represents the location of the continental shelf break, whilst the dotted line represents the 10% sea ice edge. Arrows represent the direction of flow of the energy *anomaly* – not the direction of the energy flow itself. *The total surface energy flux from open water also includes a small residual term (Supplementary Figure 2) which is not shown here.
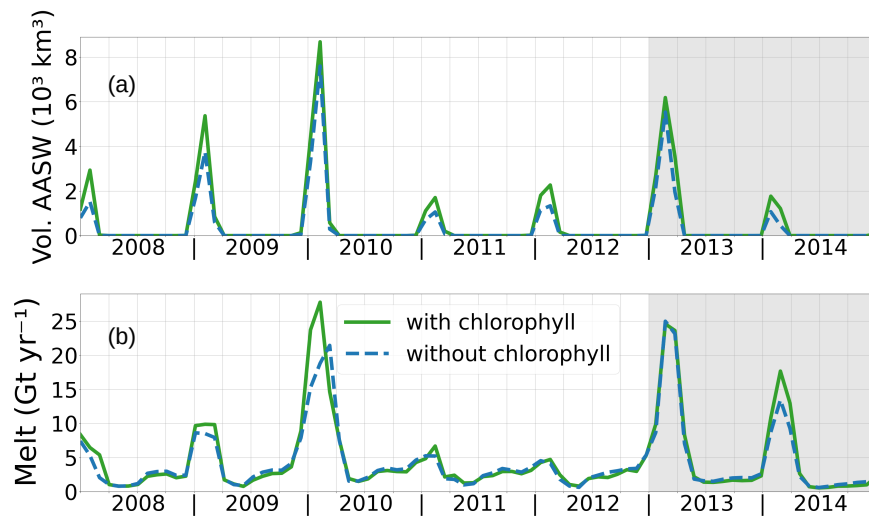
Figure 7.   Time series showing the total volume of Antarctic Surface Water (AASW; defined by temperature $> 0°$C and salinity < 34.0 g kg^{-1}) on the continental shelf (a) and the total meltwater flux from the upper 50 m of ice shelves (b), for the *GREEN* and *BLUE* experiments.
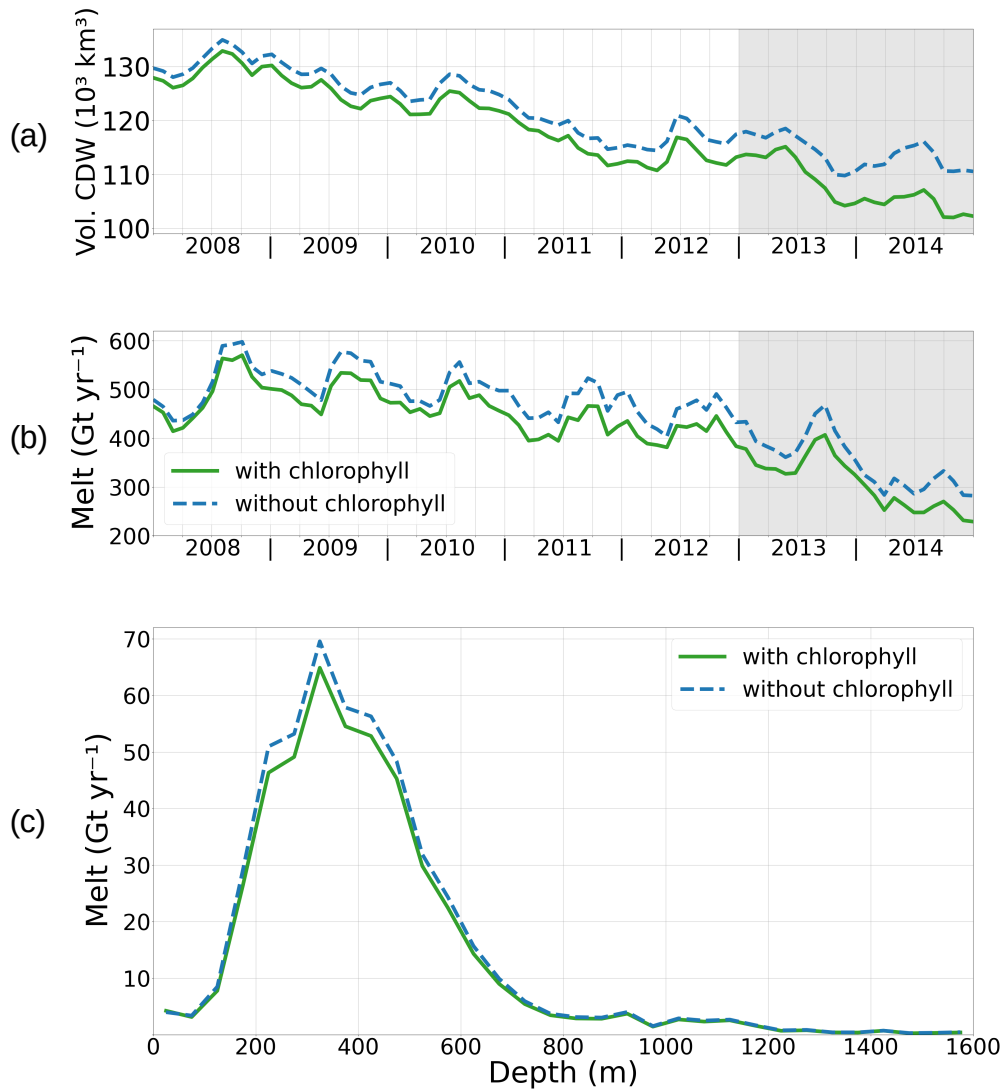
Figure 8. Time series showing the total volume of Circumpolar Deep Water (CDW; defined by temperature $> 0°$C and salinity > 34.5 g kg^{-1}) on the continental shelf (a) and the total meltwater flux from below 50 m on the ice shelves (b), for the *GREEN* and *BLUE* experiments. Grey shading marks the period of anachronistic convection. Also the ice shelf melt rate anomaly variation with respect to depth, shown here by binning over 50 m intervals (c).
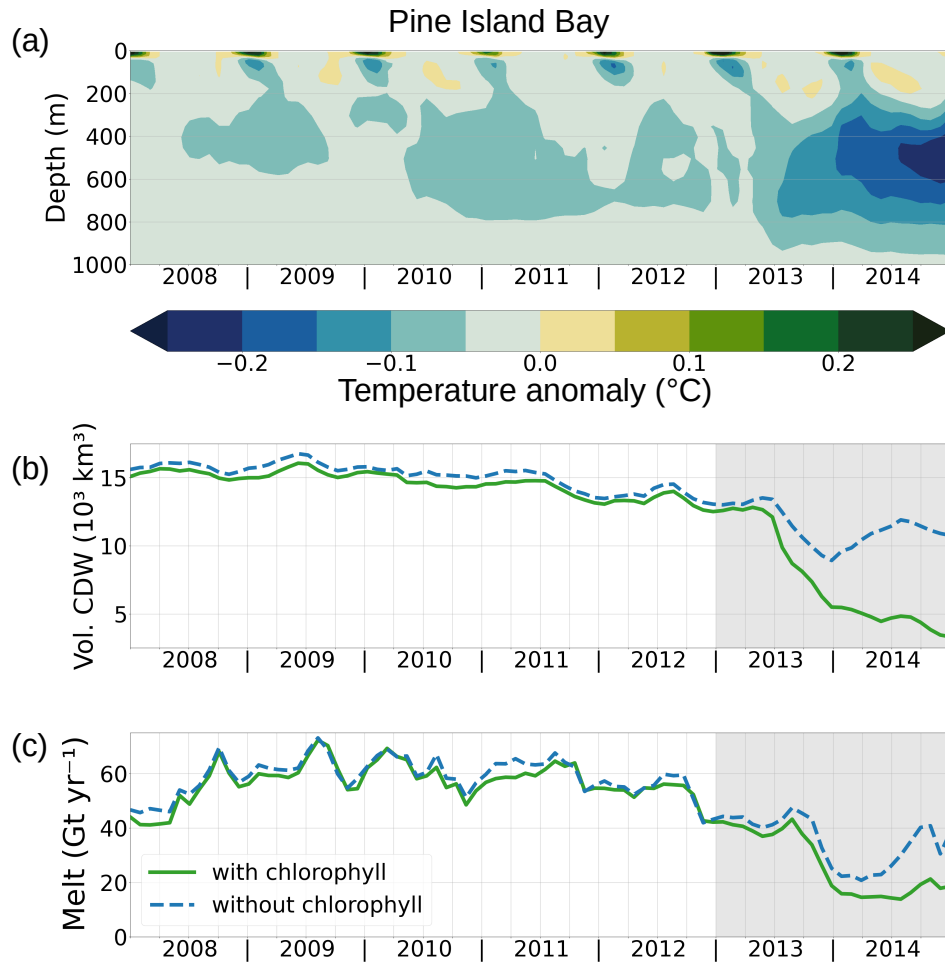
Figure 9. Hovmöller diagram (a) showing the evolution of the Pine Island Bay temperature anomaly in $GREEN$ with respect to the $BLUE$ experiment and time series showing the total volume of CDW in Pine Island Bay (b) and the total meltwater flux from ice shelves fringing Pine Island Bay (c). Grey shading marks the period of anachronistic convection.